Journal of Applied Physics

RESEARCH ARTICLE | NOVEMBER 20 2025

# Development of interatomic potential and effect of ordering on defect properties in CrMnV

Gaurav Arora ; Muhammad Waqas Qureshi; Nicholas Crnkovich ; Adrien Couet ; Kavin Ammigan ; Izabela Szlufarska ; Frederique Pellemoine



*J. Appl. Phys.* 138, 195103 (2025)
https://doi.org/10.1063/5.0302848









AIP Publishing

Journal of Applied Physics ARTICLE pubs.aip.org/aip/jap

# Development of interatomic potential and effect of ordering on defect properties in CrMnV

Cite as: J. Appl. Phys. **138**, 195103 (2025); doi: 10.1063/5.0302848
Submitted: 17 September 2025 · Accepted: 3 November 2025 ·
Published Online: 20 November 2025

View Online Export Citation CrossMark

Gaurav Arora,[1] Muhammad Waqas Qureshi,[2] Nicholas Crnkovich,[3] Adrien Couet,[3] Kavin Ammigan,[1] Izabela Szlufarska,[2,a)] and Frederique Pellemoine[1,a)]

## AFFILIATIONS

[1]Fermi National Accelerator Laboratory, Batavia, Illinois 60510, USA
[2]Department of Materials Science and Engineering, University of Wisconsin-Madison, Madison, Wisconsin 53706, USA
[3]Department of Nuclear Engineering and Engineering Physics, University of Wisconsin-Madison, Madison, Wisconsin 53706, USA

[a)]**Authors to whom correspondence should be addressed:** szlufarska@wisc.edu and fpellemo@fnal.gov

## ABSTRACT

Developing materials that can withstand extreme environments, such as high radiation doses and elevated temperatures, is crucial for next-generation particle accelerators, including the 2.4 MW Long-Baseline Neutrino Facility. High-Entropy Alloys have emerged as promising candidates for beam window materials due to their superior mechanical strength, corrosion resistance, and radiation tolerance. In this study, we focus on the Cr–Mn–V alloy system, developing and employing machine-learning interatomic potentials (MLIPs) to investigate the formation of an ordered phase and its influence on defect properties. Using hybrid Monte Carlo-Molecular Dynamics simulations, we observe the formation of a B2-ordered phase at lower temperatures, consistent with Density Functional Theory (DFT) predictions. Ordered structures display a bimodal distribution of migration energies and reduced mean square displacement values, indicating suppressed vacancy diffusion. Our results also show that the migration energy barrier varies based on the atomic species, with Mn and V exhibiting the highest and lowest average barriers, respectively. These findings suggest that atomic ordering inhibits defect mobility, potentially enhancing the radiation resistance of CrMnV alloys. The validated MLIP provides a reliable framework for simulations that are faster than traditional DFT while maintaining the accuracy required to study defect and ordering properties.





## INTRODUCTION

Developing materials capable of withstanding extreme environments, such as high radiation doses, elevated temperatures, or both, presents a significant challenge. In the context of high-energy physics, developing materials that can sustain particle beam intensities exceeding $10^{14}$ protons per second is critical for the design of next-generation particle accelerators, such as the 2.4 MW Long-Baseline Neutrino Facility (LBNF).[1,2] Beam windows, crucial components that separate different environments along the accelerator beam lines, allow particle beams to pass through with minimal energy loss. Currently, materials such as beryllium, titanium alloys, stainless steels, and aluminum alloys are used for beam windows.[3] While these materials can withstand the beam power of today's accelerators, future accelerators, which would operate at higher compared to current power levels, may exceed capabilities such as thermal stress, fatigue, and radiation damage of these materials.[3] This would limit the lifetime of the conventional materials. Thus, it is essential to study and develop materials for beam windows that could withstand the high power from next-generation particle accelerators.[2]

One such class of alloys, known as High-Entropy Alloys (HEAs), offers a promising avenue for developing beam window materials for next-generation high-power accelerators. Unlike traditional alloys, which rely on one or two principal elements, HEAs comprise multiple principal elements in near-equal concentrations. This unique composition can lead to superior properties, including higher mechanical strength,[4–9] improved corrosion resistance,[10–12] and enhanced radiation resistance[13–16] when compared with conventional alloys. It is well documented that body-centered cubic (ferritic/martensitic) alloys generally show lower void swelling and reduced embrittlement than face-centered cubic (austenitic) alloys under comparable irradiation conditions.[17–20] Low density and low

activation of materials are also necessary to minimize the loss of beam power during operation and ensure safe handling during maintenance. Thus, based on these criteria, we explored the behavior of the equimolar three-component alloy CrMnV.[21] This alloy is particularly attractive due to its low density, low activation of constituent elements, and its reported formation of a single BCC phase over a wide range of temperatures.[19]

HEAs were initially considered as random solid solutions with a homogeneous distribution of elements on lattice sites due to inherently high configurational entropy.[22,23] However, multiple studies have shown the formation of short-range (SRO) or long-range (LRO) ordered phases, which significantly influence critical properties including mechanical properties[24] (e.g., ductility, yield strength), defect formation[25] (e.g., vacancy formation and migration energies, stacking fault energies), and thermodynamic properties[26–31] (e.g., order–disorder transition temperature and heat capacity). Radiation resistance is inherently related to the stability and mobility of defects. Materials with good radiation resistance tend to promote the annihilation and recombination of defects. Migration energy governs the mobility of defects. At the timescale relevant to the initial defect creation and evolution, higher migration barriers imply a lower probability for nascent defects to drift away from their creation sites. This results in an increasing localized annihilation rate through prompt recombination, thereby reducing the population of free defects available to combine and form larger defects in the long run. Thus, migration barriers can be used as one of the parameters for assessing the radiation tolerant property of a material.[30,32,33]

Multiple studies have shown that ordering in multi-component alloys can have a significant impact on the diffusion of defects, especially on vacancy diffusion.[34–37] Despite the clear importance of ordering, there have been conflicting reports in the literature regarding its precise impact on defect mobility in multi-component alloys. For instance, a study by Ibrahim *et al.* on CoNiCrFe HEA showed that the formation of a local chemical order resulted in the suppressed diffusion of vacancies.[38] Another study by Zhou *et al.* showed the ordered phase to be more radiation resistant than the random phase. The observed behavior was attributed to the increased vacancy migration barrier in the ordered phase compared to the random phase.[39] Similarly, a study by Liu *et al.* on a CrFeNi alloy system also demonstrated that the formation of local ordering increased the vacancy migration barrier.[40] Higher migration barriers make it difficult for vacancies to aggregate and form larger vacancy clusters and stacking-fault tetrahedra. This reduction in the formation of such detrimental defect structures has been shown to increase the radiation resistance of the material.[30,40] Conversely, a recent study on the HfNbTaZr alloy system concluded that the formation of a short-range order had no significant effect on the average vacancy migration barrier, reporting similar average values for random and ordered alloys.[41] Another study by Pang *et al.* showed that the random phase was more radiation tolerant compared to the ordered phase and attributed chemical complexity behind such observation.[42] This discrepancy highlights a fundamental gap in fully understanding the complex role of chemical short-range order (CSRO) across diverse HEA systems and underscores the need for more in-depth analyses to provide generalizable insights beyond specific compositions. Understanding the significant influence of vacancy diffusion on both the short-term and long-term responses of materials under irradiation is crucial.[43] Our study aims to bridge the existing knowledge gap regarding the universal impact of a short-range chemical order (CSRO) on vacancy migration in high-entropy alloys (HEAs), particularly in the CrMnV alloy, where this effect and its fundamental mechanisms have not been previously investigated.

To address the above questions and systematically investigate the influence of atomic ordering on the vacancy diffusion behavior in CrMnV,[21] we performed calculations utilizing Density Functional Theory (DFT), Molecular Dynamics (MD), and hybrid Monte Carlo-Molecular Dynamics (MCMD). While DFT is highly accurate, its computational expense limits its application to only small system sizes.[44] An alternative and highly effective approach for modeling the formation of ordered phases at different temperatures and accurately describing the defect energy landscape in CrMnV alloys is the use of machine-learning interatomic potentials (MLIPs). MLIPs are fitted using the data obtained from multiple DFT simulations, enabling us to study larger systems without a drastic loss of accuracy.[45,46] Overall, this work develops and leverages a novel MLIP for the CrMnV alloy system to systematically investigate the role of temperature in the formation of an ordered structure and further study its impact on the migration barriers of vacancies.

## METHODOLOGY

### Development of MLIP

Multiple software packages are available for developing MLIPs.[26,47–49] We use a software package called "MLIP package: moment tensor potential (mtp)" developed by Novikov *et al.* because of its high accuracy by training with small datasets, systematic construction, easy approach for using the package, ability to provide rotation-covariance, and capability of training it on multiple computing cores.[48,50,51] Prior work validates this package for calculating vacancy barriers, defect energetics, and diffusivity in metallic and ordered systems.[52–54] Moment tensor potentials were trained with $R_{cut} = 5$ Å and $R_{min} = 2$ Å, radial basis size $n_r = 8$, radial function count of 6, and a basis of 4991 invariant moments. To ensure the generality of the interatomic potential, we ran multiple DFT simulations collecting the forces and energies to be fed into the model for training the MLIP. The training data include the unary, binary, and ternary systems. Unary compositional training data included pure Cr, Mn, and V. For each binary system, i.e., Cr–Mn, Mn–V, and Cr–V, compositions of the form $A_xB_{1-x}$ were generated with x ranging from 10 to 90 at. % at intervals of 10 at. %. This resulted in a total of nine different compositions for each binary system. For the ternary system, we included data for the equimolar structures of CrMnV. In total, 31 compositions were included in the training data: 3 unary, 27 binaries (9 for each of the 3 binary systems), and 1 ternary. Two different system sizes, containing 54 and 128 atoms, were used to ensure variability in the data, resulting in 62 unique starting cell structures. Details regarding the number and the type of simulations are provided in Table I. All starting cell structures were constructed using the Special Quasi-random Structure (SQS) technique implemented within the ATAT package.[55]

This approach led to the generation of approximately 16 500 structures with a wide range of information about local structures,

**TABLE I.** The type and the number of simulations performed during training of the MLIP. Defect simulations were run only using supercells with 128 atoms to avoid the spurious effects of periodic boundary interactions.

| Simulation type | Total number of simulations |
|---|---|
| Full relaxation of initial structures | 62 (62 structures) |
| Uniaxial 25 strained structures with strain ranging from −8% to +8% | 1550 (62 structures × 25) |
| Approximately 80 structures were generated using *Ab Initio* Molecular Dynamics (AIMD) simulations with temperature ranging from 10 until 2000 K with time step interval of 100 fs | 4960 (62 structures × 80) |
| Approximately 80 structures each were generated using AIMD simulations including defects such as single vacancy, di-vacancy, tri-vacancy, and single interstitial | 9920 [31 structures × 4 (different types) × 80] |

energies, and forces. Furthermore, the data were divided into 80–20 ratio, where 80% was used for training while 20% was used for testing purposes.[56,57]

## Input parameters for DFT

DFT calculations were performed using the Vienna *Ab initio* Simulation Package (VASP).[58,59] Ion–electron interaction described by the full potential frozen-core projector-augmented wave (PAW)[60] and the GGA-PBE54[61] exchange-correlation functional was used. The Brillouin zone was sampled using the Monkhorst–Pack method with a mesh size of 0.04 $Å^{-1}$ in reciprocal space resulting in $2\times2\times2$ and $3\times3\times3$ KPOINTS for $4\times4\times4=128$ and $3\times3\times3=54$ atom systems, respectively. The energy cutoff of 350 eV is used for the plane-wave basis set with energy and force convergence set to $10^{-4}$ eV and $10^{-2}$ eV/Å, respectively. We verified convergence against a tight reference with ENCUT = 600 eV and EDIFF = $1\times10^{-6}$. Holding ENCUT = 350 eV and tightening EDIFF from $1\times10^{-4}$ to $1\times10^{-6}$ changed the energy by only 0.147 meV/atom. Conversely, at EDIFF = $1\times10^{-4}$, increasing ENCUT from 350 to 600 eV altered the energy by 1.36 meV/atom. Both are within the commonly accepted ∼1–2 meV/atom tolerance, so we adopt ENCUT = 350 eV and EDIFF = $1\times10^{-4}$ for production. All calculations are performed using the spin-polarized effect in place. The Methfessel–Paxton technique with a smearing width of 0.1 eV is employed for electronic relaxation.

## Atomistic simulations

Molecular dynamics (MD) and hybrid MCMD simulations were carried out using the Large-scale Atomic/Molecular Massively Parallel Simulator (LAMMPS) package.[62] Hybrid MCMD was performed at 300, 500, 800, 1200, and 1500 K to get different degrees of local ordering. Periodic boundary conditions were applied in all three spatial directions. In the MCMD simulation, atoms were swapped, and potential energies were monitored to indicate whether the equilibrium states had been reached. Structures generated at different temperatures resulted in different degrees of short-range order. These structures were subsequently used to calculate migration energies and mean square displacement (MSD) of a vacancy. Details regarding the methodology used for calculating migration barriers and MSD are provided later in the text.

For quantifying the degree of ordering, we computed the Warren–Cowley parameter (WCP)[63] $\alpha_{ij}$ for each pair of elements, which is defined as follows:

$$\alpha_{ij} = 1 - \frac{P_{ij}}{x_j}. \tag{1}$$

Here, $\alpha_{ij}$ is WCP for pair *i*–*j*. $P_{ij}$ is a conditional probability of finding an atom of type *j* as the nearest neighbor of an atom of type *i*, and $x_j$ are atomic fractions of species *j* in the atomic system under consideration. WCP parameter $\alpha_{ij}=0$ corresponds to a random distribution of *j* atoms around type *i*. $\alpha_{ij}>0$ and <0 represent clustering and ordering for unlike pair of atoms, respectively.

We also quantified B2-type chemical ordering using simulated powder XRD patterns generated in VESTA[64] (Cu Kα, λ = 1.5406 Å). After summing symmetry-equivalent reflections, each pattern was normalized to its own bcc (110) fundamental to enable the comparison of relative superlattice intensities across different structures. As expected for a random bcc (A2) alloy, the (100) and (111) superlattice reflections are essentially absent, whereas in the B2-ordered case, both become visible (100), clearly observable, and (111) typically weaker, providing a sensitive signature of the chemical order.[65,66]

The energy barriers for the migration of vacancies were determined using the Climbing Image Nudged Elastic Band[67] (CI-NEB) method and the QuickMin damped minimization algorithm available in LAMMPS. The spring constant was set to 5 $eV/Å^2$. The convergence criteria for energy and force were set to $10^{-8}$ eV and $10^{-4}$ eV/Å, respectively. A total of 16 intermediate images were employed to compute each energy barrier, defined as the energy difference between the saddle point and the initial configuration. The migration energy barriers were calculated for multiple sites to ensure capturing enough statistic and distinct local atomic environments.[68] Details regarding the number of calculations are provided in the Results section.

MD calculations were carried out to compute the MSD at 1500 K for structures with different degrees of SRO. Detailed information about structure generation is given in the Results section. A vacancy was introduced in each structure for calculating MSD. Structures with introduced vacancy were relaxed using the conjugate gradient minimization technique. Temperature was slowly raised using the isothermal–isobaric ensemble (NPT; also represents a constant number of atoms, pressure, and temperature) to 1500 K, followed by MD simulation at 1500 K for 5 ns; during which time, MSD was calculated. MSD is an effective tool for understanding the movement of defects, formation of defects, and to compute diffusivities.[30]

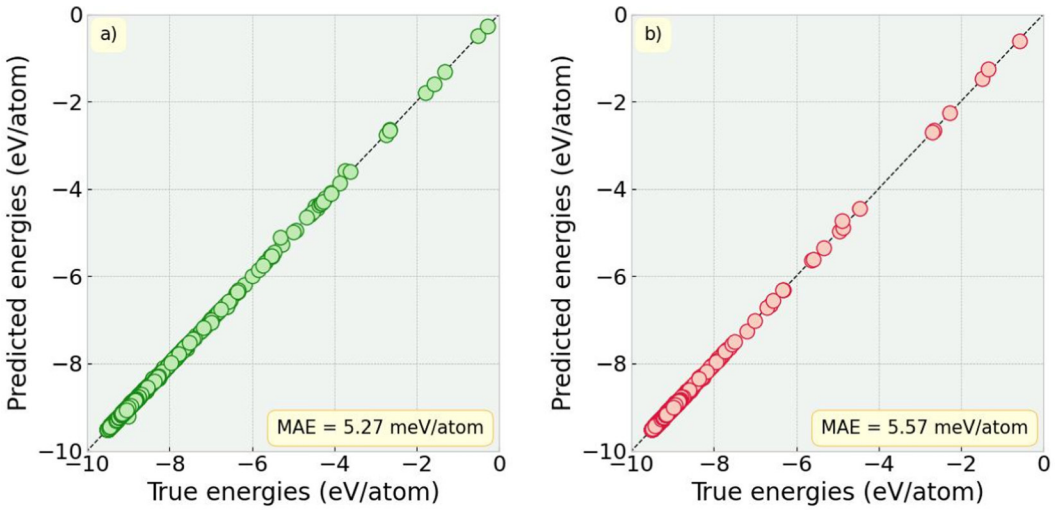


**FIG. 1.** Validating the developed MLIP against DFT energies. These plots compare DFT-calculated total energies (X axis) with MLIP-predicted total energies (Y axis). (a) shows the MLIP's performance on training data and (b) shows the MLIP's performance on testing data.

## RESULTS AND DISCUSSION

### Validation of the developed MLIP

The developed MLIP was validated as follows. As mentioned earlier, 80% of the data were used for training the model and 20% for testing the potential's accuracy. Figure 1 presents the results of accuracy for the developed potential. It shows a unity slope between the true and predicted energies, indicating an excellent fit. The X and Y axes refer to true energies calculated using DFT and predicted energies calculated using the MLIP package, respectively. The mean absolute errors (MAEs) between true and predicted energies are 5.27 meV/atom for training data and 5.57 meV/atom for test data. For forces, the calculated MAE is 0.065 eV/Å for training data and 0.067 eV/Å for test data. The accuracy of this MLIP is comparable to other recent works,[26,28,69] indicating its potential use for further study.

Additional validation for the developed potential was performed by calculating formation enthalpies for various phases and comparing them with DFT-calculated energies. All stable phases for the CrMnV system were extracted using the Materials Project (MP) phase diagram application.[70] Subsequently, the formation enthalpy was calculated for each of these phases using our developed potential within LAMMPS. Figure 2 presents a comparison between these potential-calculated energies and the corresponding DFT values. The X axis of Fig. 2 displays the compositional information for different alloys, while the Y axis represents the formation enthalpies for those alloys. Figure 2 clearly demonstrates that the developed potential can accurately predict the energies calculated using DFT for different phases within the CrMnV alloy phase space. Representative cell structures for these structures are provided in Table II. This comparison strengthens and validates the accuracy of the developed potential in predicting the different phases in CrMnV.

### Short-range order and its temperature dependence in CrMnV

Hybrid MCMD simulations were conducted to investigate the formation of local ordering at various temperatures, ranging from

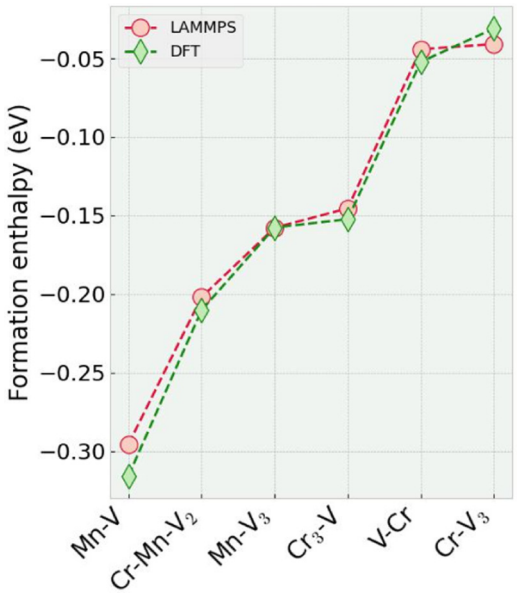


**FIG. 2.** Validation of the developed MLIP: Formation enthalpies for CrMnV different phases. Comparison of formation enthalpies calculated using the developed MLIP within LAMMPS (red circles) vs those obtained from DFT (green diamonds) for various stable CrMnV phases. Compositional information is shown on the X axis, and formation enthalpies (in eV/atom) are on the Y axis.

**TABLE II.** Structural details of CrMnV phases. This table presents the visual representations of the unit cells for the CrMnV phases analyzed in Fig. 2.

| Composition | Mn-V | Mn-$V_2$-Cr | Mn-$V_3$ | V-$Cr_3$ | V-Cr | $V_3$-Cr |
|---|---|---|---|---|---|---|
| Representative cell (Mn, V, Cr) |  | 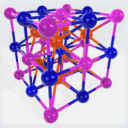 | 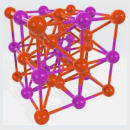 | 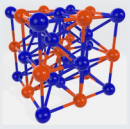 |  | 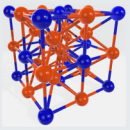 |

300 to 1500 K, using a 1024-atom system. For each simulation, a structure with randomly distributed Cr–Mn–V on lattice sites served as the starting configuration. Before initiating the hybrid MCMD simulations (which involve atom swapping), each structure was brought to equilibrium. This was achieved by first running an NPT ensemble (isothermal–isobaric) MD simulation for 10 ps, followed by an NVE ensemble (microcanonical; also represents a constant number of atoms, constant volume, and energy of the system) MD simulation for 5 ps. The temperature was monitored during NVE simulations to ensure that the system had equilibrated to the desired temperature for the subsequent hybrid MCMD run. For NPT pre-equilibration, we used a Nosé–Hoover thermostat and an anisotropic Nosé–Hoover barostat, with temperature damping Tdamp of 0.1 ps and pressure damping Pdamp of 0.5 ps with a target pressure of 0 bar. The evolution of the system's potential energy with respect to MC steps for different temperatures is presented in Fig. 3. The X axis represents the number of MC steps, while the Y axis shows the potential energy in eV/atom. For each simulation, the potential energy was normalized against the system's initial potential energy.

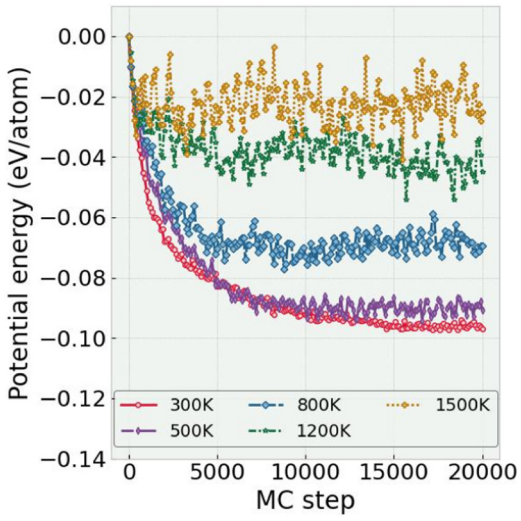


**FIG. 3.** Evolution of potential energy during hybrid MCMD simulations at various temperatures.

Figure 3 clearly illustrates that at lower temperatures (300 and 500 K), the system's potential energy decreases by approximately 0.09 eV/atom compared to the energy of the starting configuration. This significant reduction indicates that atom positions have changed, and the system has found a new equilibrium corresponding to a different, possibly ordered structure compared to the starting configuration.[71] Conversely, for simulations run at 1500 K, the total decrease in potential energy from the same initial structure is only about 0.02 eV/atom, which is approximately five times lower than that observed at 300 K. This suggests that at higher temperatures, the structure undergoes minimal changes from its initial state, hindering the formation of a significant order in the system.

To quantify the degree of short-range order or clustering, the Warren–Cowley Parameter (WCP) was employed. The final structures obtained after running hybrid MCMD were further analyzed to study the formation of order within the system. These final structures were fully relaxed using LAMMPS to negate the effect of lattice expansion due to temperature before calculating the WCP. Figure 4(a) shows the calculated WCP for all pairs of atoms at different temperatures. As the temperature increases, the WCP value for all pairs tends toward zero, indicating an increase in randomness. The highly negative value for Mn–V and Cr–Cr pairs signifies the formation of an ordered structure containing Mn–V layered structures and clustering of Cr, respectively, consistent with the slice of atomic configuration shown in Fig. 4(b).[41] This ordering is more pronounced in structures simulated at lower temperatures, particularly at 300 K. Further visual investigation of the final structures revealed the formation of an ordered B2 structure, characterized by alternating layers of Mn and V. A basic supercell of a B2 phase is depicted in Table II with Mn–V composition. Along with the Mn–V B2 phase, we also observe the Cr cluster formation. Clustering of Cr has also been observed in other atomic systems.[40,72] We further quantified B2 ordering using simulated powder x-ray diffraction (XRD). Figure 5(a) shows patterns for the random, semi-ordered, and ordered structures using Cu Kα, $\lambda = 1.5406$ Å, each normalized to its bcc (110) fundamental. Because the B2 superlattice reflections (100) and (111) occur near $2\theta \approx 31.2°$ and 55.7°, respectively, and are much weaker than (110), we provide magnified views in Figs. 5(b) and 5(c), respectively.[65] The ordered structure exhibits the strongest superlattice peaks, the semi-ordered model is intermediate, and the random

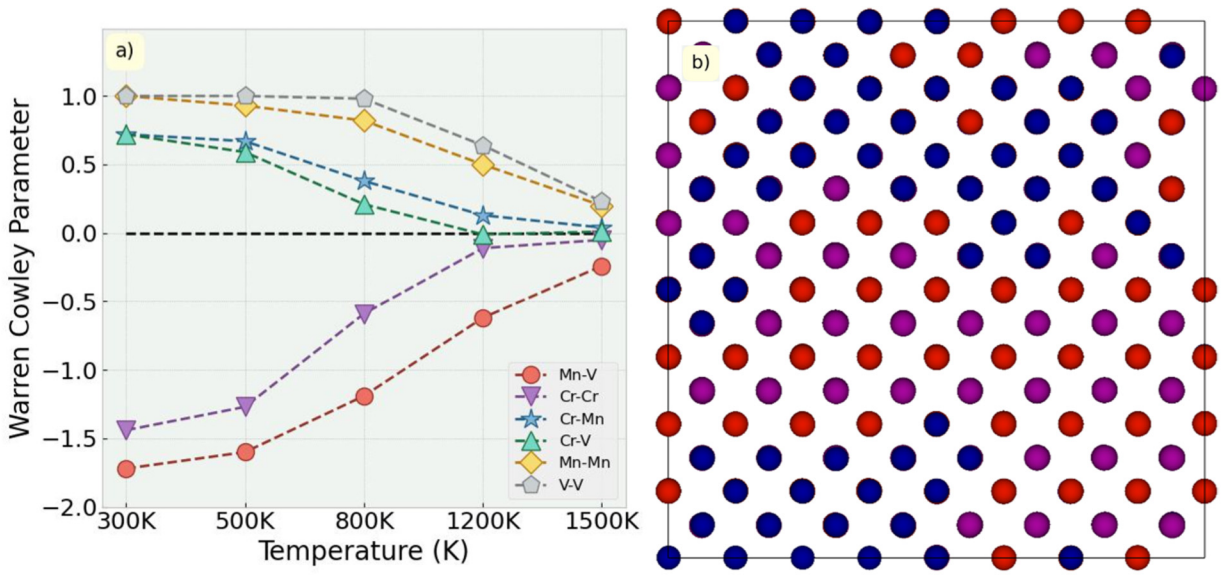


**FIG. 4.** (a) Temperature dependence of Warren–Cowley Short-Range Order (WCP) Parameters for Cr–Mn–V pairs. Negative WCP values indicate a preference ordering for Mn–V (unlike pair) and clustering for Cr (like pair). (b) Final atomic configuration of CrMnV run at 300 K.

alloy is essentially zero at these positions, consistent with B2 selection rules. Figure 5(d) summarizes this trend via the intensity ratios $I_{100}/I_{110}$ and $I_{111}/I_{110}$, which increase monotonically with the degree of chemical order.

We further validated the relative stability of the formed structure, containing the B2 phase along with Cr clusters, by comparing its enthalpy with that of the initial random structure. The energies of these structures were calculated using the developed MLIP within LAMMPS and, subsequently, compared against DFT-calculated energies. For DFT calculations, a smaller structure containing 128 atoms was utilized. Hybrid MCMD simulations using LAMMPS were employed to generate various intermediate structures exhibiting different degrees of ordering. These extracted structures were then fully relaxed using both LAMMPS (with the developed potential) and DFT. Figure 6 presents the per-atom energy comparison between DFT (green circles) and LAMMPS (red circles) for these structures. The X axis represents the Monte Carlo (MC) steps at which the intermediate structures were extracted, and the Y axis shows the per-atom energy. This comparison clearly demonstrates that the energies of different structures predicted by the MLIP using LAMMPS show good agreement with DFT. This further confirms the accuracy of our developed potential and its ability to accurately predict energies for various phases.

## Vacancy migration energy

The developed MLIP was employed to calculate the vacancy migration energies in structures with varying degrees of short-range order, allowing us to investigate the effect of ordering on the migration barrier. For each state (initial/semi-ordered/ordered), we sampled ∼2000 1NN vacancy hops by selecting ∼250 random lattice sites and evaluating hops to their first eight nearest neighbors. To achieve this, three distinct structures were selected directly from the trajectory of our previously described hybrid MCMD simulation performed at 300 K using a 1024-atom system.

1. **Initial Random Structure:** The starting configuration of the 300 K hybrid MCMD simulation, characterized by a random distribution of Cr, Mn, and V atoms on lattice sites, was chosen as the first structure to establish a baseline for vacancy migration barriers. This represents a state with minimal order.
2. **Semi-Ordered Structure:** A snapshot of the system's configuration after 5000 Monte Carlo (MC) steps of the 300 K hybrid MCMD simulation was extracted. As depicted in Fig. 3, this intermediate point shows a significant initial decrease in potential energy, indicating the onset of ordering.
3. **Fully Ordered Structure:** The final configuration obtained at the end of 20 000 MC steps from the same 300 K hybrid MCMD simulation was selected as the third structure. This structure represents the most ordered state achieved at 300 K, characterized by a substantial reduction in potential energy (Fig. 3) and pronounced short-range ordering, including B2 phase formation for Mn–V pairs and Cr clustering, as quantified by the WCP parameters and x-ray diffraction pattern. (Figures 4 and 5).

Prior to vacancy migration energy calculations, these three extracted structures were fully relaxed using the developed MLIP to ensure that they were in a stable, energy-minimized state. By analyzing these three structures, each representing a different stage of ordering evolution, we aimed to systematically study the impact of short-range order on vacancy migration barriers.

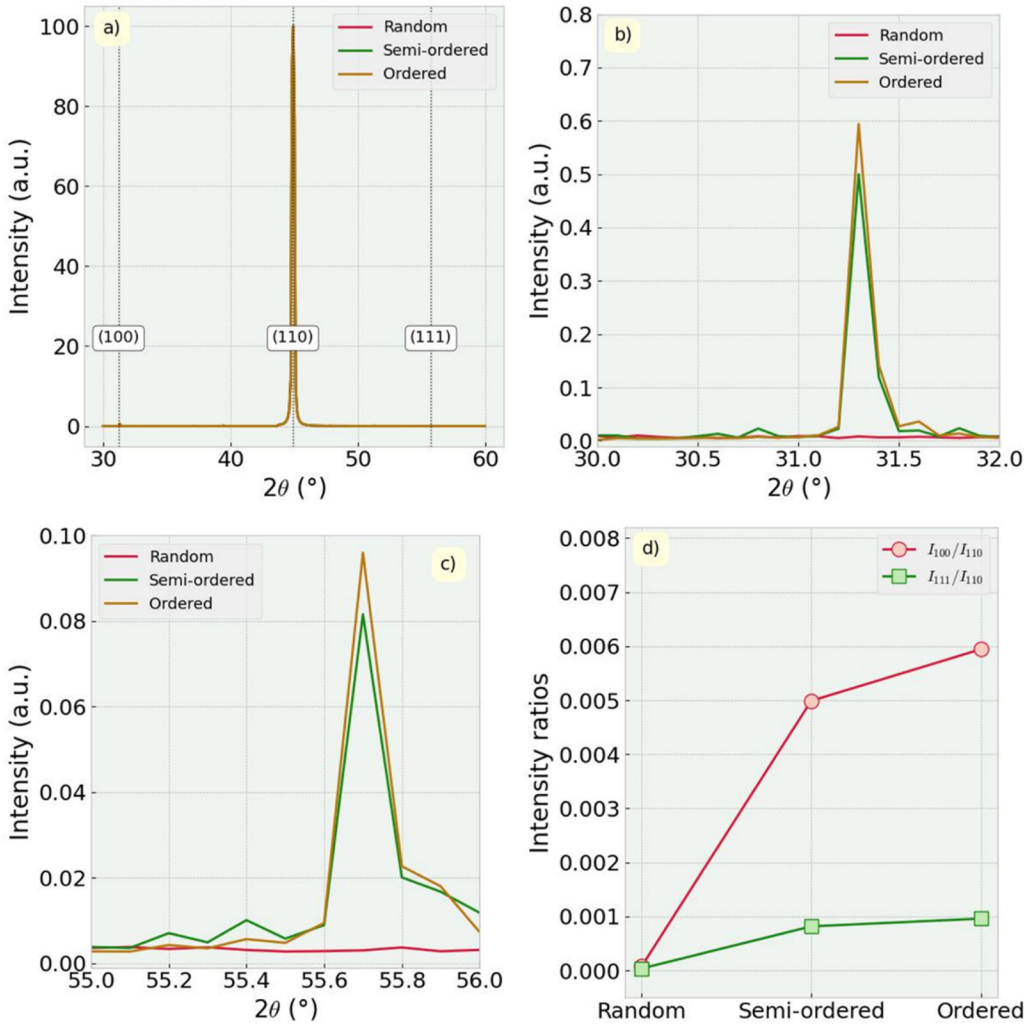


**FIG. 5.** Simulated x-ray diffraction (XRD) patterns and ordering metrics for BCC/B2 alloys (Cu Kα, λ = 1.5406 Å). (a) Full 2θ scan with thin dotted guides at B2-sensitive superlattice reflections (100) ≈ 31.2°, (111) ≈ 55.7°, and the fundamental (110) ≈ 44.9°. Intensities are normalized to the (110) fundamental. Ordered and semi-ordered alloys exhibit superlattice intensity while the random alloy shows essentially none. (b) Zoom of 30°–32° highlighting the (100) superlattice peak: strongest for the ordered alloy, weaker for semi-ordered, and negligible for random. (c) Zoom of 55°–56° showing the weak (111) superlattice peak with the same ordering trend. (d) Intensity ratios $I_{100}/I_{110}$ and $I_{111}/I_{110}$ increase monotonically from random to semi-ordered, followed by ordered, quantitatively confirming the emergence of B2-type chemical order.

Figure 7 presents the histograms of calculated vacancy migration energies for the three selected structures: (a) the initial random structure, (b) the semi-ordered structure (after 5000 MC steps at 300 K), and (c) the fully ordered structure (after 20 000 MC steps at 300 K). For each structure, approximately 2000 individual migration pathways were explored to build these distributions. The histogram for the initial random structure [Fig. 7(a)] shows a relatively broad, unimodal distribution of migration barriers, with an average migration barrier of 1.23 eV. This spread reflects the diverse local atomic environments inherent in a random solid solution. Similarly, the semi-ordered structure [Fig. 7(b)], extracted after 5000 MC steps, also exhibits a unimodal distribution, with its peak slightly shifted to approximately 1.28 eV. This modest increase in the average migration barrier from the random to the semi-ordered state suggests an initial tendency for migration barriers to increase with the onset of order, though the overall environmental diversity is not yet fundamentally altered.

A dramatic change is observed for the fully ordered structure [Fig. 7(c)], obtained after 20 000 MC steps. Here, the distribution of migration barriers becomes distinctly bimodal, presenting two prominent peaks: one at approximately 0.9–1.0 eV and another at around 1.8–1.9 eV. Quantitatively, ∼1550 of 2000 events (77.5%) lie above 1.2 eV—the average barrier of the random structure in Fig. 7(a)—while 450 events (22.5%) are ≤1.2 eV, i.e., high-barrier

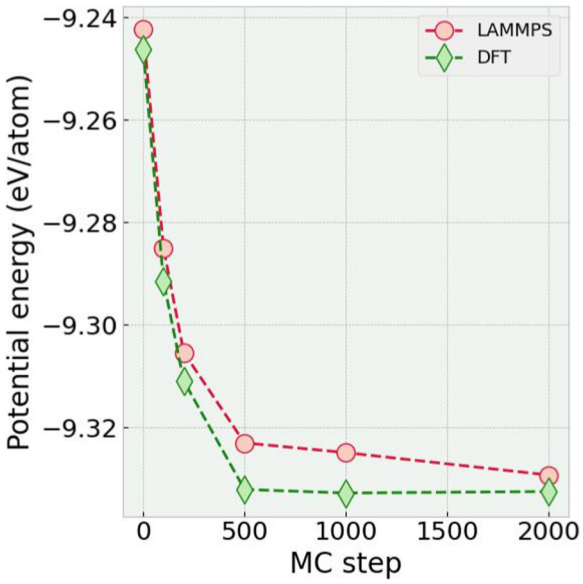


**FIG. 6.** Energy comparison of intermediate ordered structures: DFT vs MLIP predictions. Red circles and green diamonds data points, respectively, represent per atom system energy calculated using the MLIP (within LAMMPS) and DFT. One-on-one comparison clearly shows the accuracy of the potential in predicting energies for different phases.

events are ∼3.44× more frequent. This bimodal distribution is a clear signature of the formation of an ordered phase, such as the B2 structure and Cr clusters identified previously. The two distinct peaks correspond to different types of atomic environments or jump pathways that emerge due to chemical ordering. This indicates that the formation of the short-range order and, subsequently, the B2 phase, fundamentally alters the vacancy-migration landscape, creating a distribution of both lower and significantly higher activation energies compared to the disordered state. The strong skew toward higher barriers implies reduced vacancy diffusivity, which can limit the growth of larger defects and potentially enhance the radiation tolerance of the alloy. An alloy with higher average migration barriers would exhibit lower vacancy diffusion, thereby limiting the formation of larger defects and potentially enhancing the radiation tolerance of the alloy.[13,30,73] This observation highlights that reporting a single average energy, especially in an ordered alloy, does not capture the full picture across distinct atomic environments.

While the overall impact of the short-range order on the distribution of migration barriers is clear, we found no direct correlation between the migration barrier and the atomic types surrounding the vacancy site (its first-nearest neighbors) in the random alloy. This suggests that the energy landscape for a hop is influenced by the broader, often non-uniform, ordered domains rather than just the immediate neighbors. However, a more direct influence was observed when considering the identity of the atom performing the jump into the vacant site, irrespective of its surrounding environment, especially in the ordered alloy. Figure 8 presents violin plots illustrating the distribution of these element-specific migration energies in ordered alloys. Our calculations revealed distinct average migration energies depending on the atomic species making the hop: Cr atoms showed an average jump energy of 1.27 eV, Mn atoms of 1.39 eV, and V atoms of 1.05 eV, respectively. As clearly depicted in Fig. 8, the distribution for Mn jumps is notably shifted toward higher energies, implying that the motion of a Mn atom into a neighboring vacant site is energetically the most unfavorable among the three constituent elements. Conversely, V atoms face the lowest barrier for jumping into a vacancy, as shown by their distribution being centered at lower energies. A similar behavior was also observed in the random alloy, where Mn showed the highest barrier (1.39 eV) and V the lowest (1.15 eV), with the former being approximately 20% higher than the latter.



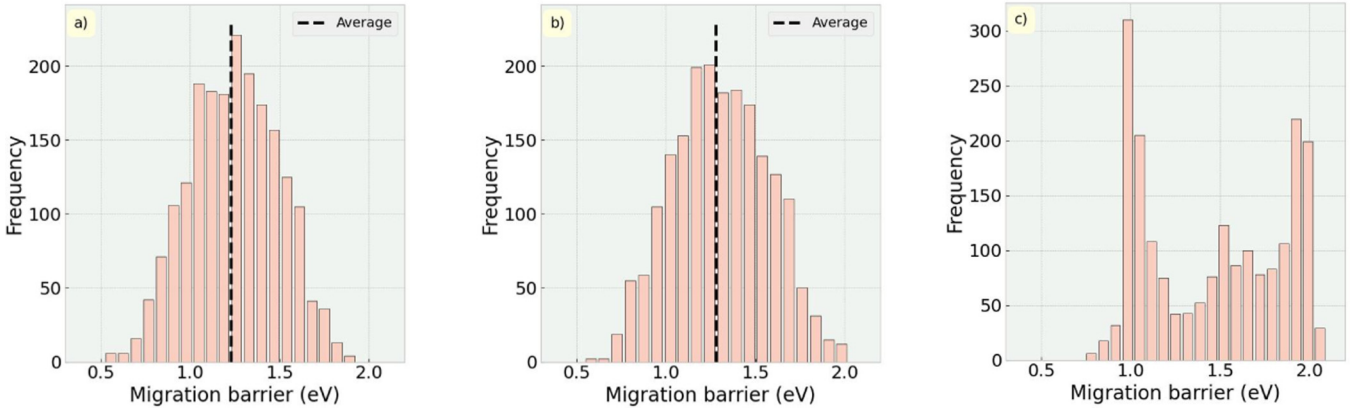


**FIG. 7.** Histograms of vacancy migration energies for different states of order. Histograms illustrate the distribution of calculated vacancy migration energies (in eV) for (a) the initial random structure, (b) the semi-ordered structure (extracted at 5000 MC steps), and (c) the fully ordered structure (extracted at 20 000 MC steps).

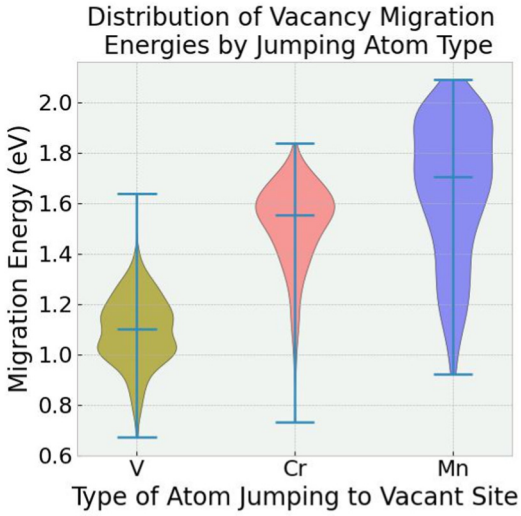


**FIG. 8.** Violin plots illustrating the distribution of calculated vacancy migration energies (in eV) for jumps performed by vanadium (V), chromium (Cr), and manganese (Mn) atoms into a vacant site for an ordered alloy.

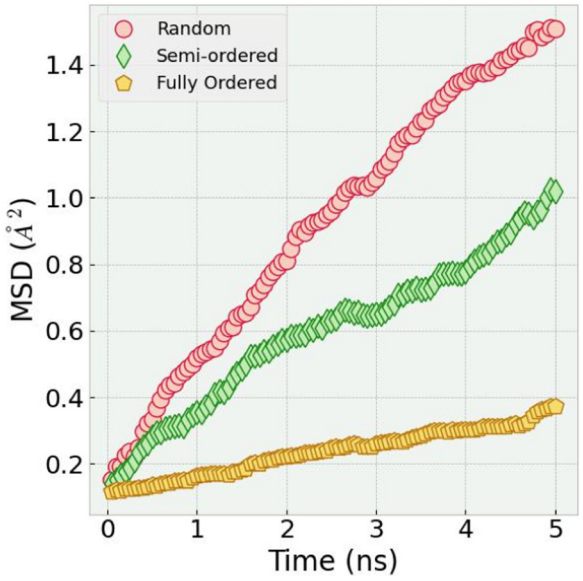


**FIG. 9.** Mean squared displacement (MSD) of CrMnV alloys at 1500 K for random (red circles), semi-ordered (green diamond), and fully ordered (yellow pentagon).

### Mean square displacement

To fully describe the macroscopic diffusion kinetics, we computed the Mean Squared Displacement (MSD) for the random, semi-ordered, and fully ordered alloys. MSD provides a direct measure of how far, on average, an atom moves from its initial position over time, thereby directly quantifying the impact of ordering on macroscopic atomic mobility and overall diffusion coefficients. Three different sets of simulations with distinct placement of a vacancy for each simulation were performed and average MSD was calculated. In particular, three independent simulations were performed with the vacancy initialized on a Cr site, a Mn site, and a V site, respectively. The MSD reported is the arithmetic mean across these placements. Figure 9 shows the computed MSD curves for vacancy-mediated diffusion in the random, semi-ordered (5000th MC step), and fully ordered (20 000th MC step) structures, all simulated at 1500 K. A clear and progressive decrease in the slope of the MSD curves is observed as the degree of order increases. The random structure (red circles) exhibits the steepest slope, indicating the highest atomic mobility and fastest diffusion. Conversely, the fully ordered structure (orange pentagons) shows the shallowest slope, signifying the most significant impediment to diffusion. This observation clearly demonstrates that the formation of an ordered phase impedes vacancy motion and, consequently, overall atomic transport.

We further analyzed these data by fitting the linear regime of each MSD curve to extract its slope, which was then used to calculate the diffusion coefficient (D) via the Einstein relation ($D = \text{slope}/6$).[74] The calculated diffusion coefficients for the random, semi-ordered, and fully ordered alloys are $4.5 \times 10^{-13}$, $2.5 \times 10^{-13}$, and $0.8 \times 10^{-13}$ $m^2/s$, respectively. This macroscopic evidence directly supports our microscopic findings from migration barrier analysis (Fig. 7), demonstrating that the presence of a short-range order, particularly the B2 phase, fundamentally alters the diffusion kinetics in CrMnV alloys, leading to significantly reduced atomic mobility.

## CONCLUSION

In this study, we successfully developed a highly accurate machine-learning interatomic potential (MLIP) for the CrMnV alloy. This potential was rigorously validated against Density Functional Theory (DFT) calculations, demonstrating an excellent agreement in predicting energies and phase stabilities, thereby enabling large-scale atomistic simulations. Our work revealed the formation of a B2-ordered phase and Cr clustering at lower temperatures such as 300 K. We demonstrated that this ordering transforms the vacancy migration energy landscape from a unimodal to a bimodal distribution, creating both lower and notably higher energy barriers. Furthermore, we showed that the type of the jumping atom strongly influences these barriers, with Mn exhibiting the highest. Mean Squared Displacement (MSD) calculations confirmed that ordering reduces atomic diffusivity. These findings collectively establish that the short-range order in CrMnV fundamentally alters vacancy diffusion kinetics, providing crucial insights for designing radiation-tolerant materials for extreme environments.

## ACKNOWLEDGMENTS

This work was produced by FermiForward Discovery Group, LLC under Contract No. 89243024CSC000002 with the U.S. Department of Energy, Office of Science, Office of High Energy Physics. Publisher acknowledges the U.S. Government license to

provide public access under the DOE Public Access Plan and Department of High energy Physics Program Grant No. DE-SC0025373. This research used resources of the National Energy Research Scientific Computing Center (NERSC), a Department of Energy User Facility using NERSC Award No. HEP-ERCAP0030984 and Fermilab Wilson computing cluster. This document was prepared with the support of the RaDIATE Collaboration using the resources of the University of Wisconsin-Madison and Fermi National Accelerator Laboratory.

## AUTHOR DECLARATIONS

### Conflict of Interest

The authors have no conflicts to disclose.

### Author Contributions

**Gaurav Arora:** Conceptualization (lead); Data curation (lead); Formal analysis (lead); Investigation (lead); Methodology (lead); Resources (lead); Validation (lead); Writing – original draft (lead); Writing – review & editing (lead). **Muhammad Waqas Qureshi:** Formal analysis (supporting); Validation (supporting); Writing – review & editing (supporting). **Nicholas Crnkovich:** Writing – review & editing (supporting). **Adrien Couet:** Writing – review & editing (equal). **Kavin Ammigan:** Funding acquisition (supporting); Writing – review & editing (supporting). **Izabela Szlufarska:** Funding acquisition (equal); Investigation (equal); Methodology (equal); Project administration (equal); Supervision (equal); Writing – review & editing (equal). **Frederique Pellemoine:** Funding acquisition (equal); Project administration (equal); Writing – review & editing (equal).

## DATA AVAILABILITY

The data that support the findings of this study are available from the corresponding authors upon reasonable request.

## REFERENCES

[1]K. Ammigan *et al.*, "Novel materials for next-generation accelerator target facilities," arXiv:2405.18545 (2024).
[2]K. Ammigan *et al.*, "Novel materials and concepts for next-generation high power target applications," arXiv:2203.08357 (2022), pp. 1–15.
[3]L. Notari, M. Pasquali, F. Carra, M. Losasso, and M. Tomut, "Materials adopted for particle beam windows in relevant experimental facilities," Phys. Rev. Accel. Beams **27**, 24801 (2024).
[4]B. Gludovatz, A. Hohenwarter, D. Catoor, E. H. Chang, E. P. George, and R. O. Ritchie, "A fracture-resistant high-entropy alloy for cryogenic applications," Science **345**, 1153–1158 (2014).
[5]E. P. George, D. Raabe, and R. O. Ritchie, "High-entropy alloys," Nat. Rev. Mater. **4**, 515–534 (2019).
[6]W. Li *et al.*, "Mechanical behavior of high-entropy alloys," Prog. Mater. Sci. **118**, 100777 (2021).
[7]Z. D. Han *et al.*, "Effect of Ti additions on mechanical properties of NbMoTaW and VNbMoTaW refractory high entropy alloys," Intermetallics **84**, 153–157 (2017).
[8]S. Jiang, D. sun, Y. Zhang, S. Wang, and C. Zhao, "Plastic deformation mechanisms of equiatomic $Ni_{20}Ti_{20}Fe_{20}Al_{20}Cu_{20}$ high-entropy alloy at high temperatures," J. Mater. Sci. **52**, 3199–3207 (2017).
[9]K. M. Youssef, A. J. Zaddach, C. Niu, D. L. Irving, and C. C. Koch, "A novel low-density, high-hardness, high-entropy alloy with close-packed single-phase nanocrystalline structures," Mater. Res. Lett. **3**, 95–99 (2014).
[10]Y. Qiu, S. Thomas, M. A. Gibson, H. L. Fraser, and N. Birbilis, "Corrosion of high entropy alloys," npj Mater. Degrad. **1**, 15 (2017).
[11]W. Zhang *et al.*, "Interface evolution and corrosion performance of (TiTaNbZrNi)N HEA coatings with a hybrid architecture under 6 MeV Au-ion irradiation," J. Nucl. Mater. **567**, 153832 (2022).
[12]Z. Zhang, E. Han, and C. Xiang, "Effect of helium ion irradiation on short-time corrosion behavior of two novel high-entropy alloys in simulated PWR primary water," Corros. Sci. **191**, 109742 (2021).
[13]C. Lu *et al.*, "Enhancing radiation tolerance by controlling defect mobility and migration pathways in multicomponent single-phase alloys," Nat. Commun. **7**, 13564 (2016).
[14]D. Chen *et al.*, "Effects of minor alloying addition on He bubble formation in the irradiated FeCoNiCr-based high-entropy alloys," J. Nucl. Mater. **542**, 152458 (2020).
[15]S. Shen *et al.*, "Irradiation damage and swelling of carbon-doped $Fe_{38}Mn_{40}Ni_{11}Al_4Cr_7$ high-entropy alloys under heavy ion irradiation at elevated temperature," J. Mater. Sci. **55**, 17218–17231 (2020).
[16]Y. Lin *et al.*, "Enhanced radiation tolerance of the Ni-Co-Cr-Fe high-entropy alloy as revealed from primary damage," Acta Mater. **196**, 133–143 (2020).
[17]F. A. Garner, M. B. Toloczko, and B. H. Sencer, "Comparison of swelling and irradiation creep behavior of fcc-austenitic and bcc-ferritic/martensitic alloys at high neutron exposure," J. Nucl. Mater. **276**, 123–142 (2000).
[18]S. J. Zinkle and G. S. Was, "Materials challenges in nuclear energy," Acta Mater. **61**, 735–758 (2013).
[19]E. J. Pickering *et al.*, "High-entropy alloys for advanced nuclear applications," Entropy **23** (2021).
[20]S. J. Zinkle and L. L. Snead, "Designing radiation resistance in materials for fusion energy," Annu. Rev. Mater. Res. **44**, 241–267 (2014).
[21]P. J. Barron *et al.*, "Towards V-based high-entropy alloys for nuclear fusion applications," Scr. Mater. **176**, 12–16 (2020).
[22]J. W. Yeh *et al.*, "Nanostructured high-entropy alloys with multiple principal elements: Novel alloy design concepts and outcomes," Adv. Eng. Mater. **6**, 299–303 (2004).
[23]Y. Zhang *et al.*, "Microstructures and properties of high-entropy alloys," Prog. Mater. Sci. **61**, 1–93 (2014).
[24]S. Dasari *et al.*, "Exceptional enhancement of mechanical properties in high-entropy alloys via thermodynamically guided local chemical ordering," Proc. Natl. Acad. Sci. U.S.A. **120**, e2211787120 (2023).
[25]G. Arora, K. D. Rawat, and D. S. Aidhy, "Effect of atomic order/disorder on Cr segregation in Ni-Fe alloys," J. Appl. Phys. **124**, 115303 (2018).
[26]P. A. Santos-Florez *et al.*, "Short-range order and its impacts on the BCC NbMoTaW multi-principal element alloy by the machine-learning potential," Acta Mater. **255**, 119041 (2023).
[27]S. Zhao, "Defect properties in a VTaCrW equiatomic high entropy alloy (HEA) with the body centered cubic (bcc) structure," J. Mater. Sci. Technol. **44**, 133–139 (2020).
[28]J. Byggmästar, K. Nordlund, and F. Djurabekova, "Modeling refractory high-entropy alloys with efficient machine-learned interatomic potentials: Defects and segregation," Phys. Rev. B **104**, 1–11 (2021).
[29]X. Zhou, S. He, and J. Marian, "Vacancy energetics and diffusivities in the equiatomic multielement Nb-Mo-Ta-W alloy," Materials **15**(15), 5468 (2022).
[30]G. Arora, G. Bonny, N. Castin, and D. S. S. Aidhy, "Effect of different point-defect energetics in Ni80X20 (X = Fe, Pd) on contrasting vacancy cluster formation from atomistic simulations," Materialia **15**, 100974 (2021).
[31]Y. Wu, Z. Li, H. Feng, and S. He, "Atomic interactions and order–disorder transition in FCC-type $FeCoNiAl_{1-x}$ $Ti_x$ high-entropy alloys," Materials **15**, 3992 (2022).
[32]G. R. Lumpkin *et al.*, "Experimental and atomistic modeling study of ion irradiation damage in thin crystals of the $TiO_2$ polymorphs," Phys. Rev. B **77**, 214201 (2008).

[33]N. Swaminathan, D. Morgan, and I. Szlufarska, "Role of recombination kinetics and grain size in radiation-induced amorphization," Phys. Rev. B: Condens. Matter Mater. Phys. **86**, 214110 (2012).
[34]C. Gao, S. Wang, X. Liu, and C. V. Singh, "Defect energetics in an high-entropy alloy fcc CoCrFeMnNi," Mater. Adv. **5**, 4231–4241 (2024).
[35]G. Arora and D. Aidhy, "Segregation and binding energetics at grain boundaries in fluorite oxides," J. Mater. Chem. A **5**(8), 4026–4035 (2017).
[36]M. Mizuno, K. Sugita, and H. Araki, "Defect energetics for diffusion in CrMnFeCoNi high-entropy alloy from first-principles calculations," Comput. Mater. Sci. **170**, 109163 (2019).
[37]S. L. Thomas and S. Patala, "Vacancy diffusion in multi-principal element alloys: The role of chemical disorder in the ordered lattice," Acta Mater. **196**, 144–153 (2020).
[38]S. A. Ibrahim *et al.*, "Effect of local chemical order on monovacancy diffusion in CoNiCrFe high-entropy alloy," J. Nucl. Mater. **601**, 155335 (2024).
[39]Y. H. Zhou *et al.*, "Tailoring the radiation tolerance of eutectic high-entropy alloy via phase-composition control," J. Nucl. Mater. **584**, 154561 (2023).
[40]L. Liu *et al.*, "Local chemical ordering and its impact on radiation damage behavior of multi-principal element alloys," J. Mater. Sci. Technol. **135**, 13–25 (2023).
[41]A. Manzoor and Y. Zhang, "Influence of defect thermodynamics on self-diffusion in complex concentrated alloys with chemical ordering," JOM **74**, 4107–4120 (2022).
[42]J. Pang *et al.*, "Atomic scale structure dominated FCC and B2 responses to He ion irradiation in eutectic high-entropy alloy $AlCoCrFeNi_{2.1}$," J. Mater. Sci. Technol. **129**, 87–95 (2022).
[43]A. Shirinyan and Y. Bilogorodskyy, "Effect of radiation-induced vacancy saturation on the first-order phase transformation in nanoparticles: Insights from a model," Beilstein J. Nanotechnol. **15**, 1453–1472 (2024).
[44]G. Arora, A. Manzoor, and D. S. Aidhy, "Charge-density based evaluation and prediction of stacking fault energies in Ni alloys from DFT and machine learning," J. Appl. Phys. **132**, 225104 (2022).
[45]R. Ramprasad, R. Batra, G. Pilania, A. Mannodi-Kanakkithodi, and C. Kim, "Machine learning in materials informatics: Recent applications and prospects," npj Comput. Mater. **3** (2017).
[46]Y. Mishin, "Machine-learning interatomic potentials for materials science," Acta Mater. **214**, 116980 (2021).
[47]A. Singraber, T. Morawietz, J. Behler, and C. Dellago, "Parallel multistream training of high-dimensional neural network potentials," J. Chem. Theory Comput. **15**, 3075–3092 (2019).
[48]I. S. Novikov, K. Gubaev, E. V. Podryabinkin, and A. V. Shapeev, "The MLIP package: Moment tensor potentials with MPI and active learning," Mach. Learn.: Sci. Technol. **2**, 025002 (2020).
[49]A. Khorshidi and A. A. Peterson, "Amp: A modular approach to machine learning in atomistic simulations," Comput. Phys. Commun. **207**, 310–324 (2016).
[50]E. V. Podryabinkin and A. V. Shapeev, "Active learning of linearly parametrized interatomic potentials," Comput. Mater. Sci. **140**, 171–180 (2017).
[51]Y. Zuo *et al.*, "Performance and cost assessment of machine learning interatomic potentials," J. Phys. Chem. A **124**, 731–745 (2020).
[52]I. I. Novoselov, A. V. Yanilkin, A. V. Shapeev, and E. V. Podryabinkin, "Moment tensor potentials as a promising tool to study diffusion processes," Comput. Mater. Sci. **164**, 46–56 (2019).
[53]K. Zongo, H. Sun, C. Ouellet-Plamondon, and L. K. Béland, "A unified moment tensor potential for silicon, oxygen, and silica," NPJ Comput. Mater. **10** (2024).
[54]J. Wang *et al.*, "Efficient moment tensor machine-learning interatomic potential for accurate description of defects in Ni-Al alloys," Phys. Rev. Mater. **9**, 53805 (2025).
[55]A. van de Walle *et al.*, "Efficient stochastic generation of special quasirandom structures," Calphad **42**, 13–18 (2013).
[56]G. Arora and D. S. Aidhy, "Machine learning enabled prediction of stacking fault energies in concentrated alloys," Metals **10**, 1072 (2020).
[57]G. Arora, S. Kamrava, P. Tahmasebi, and D. S. Aidhy, "Charge-density based convolutional neural networks for stacking fault energy prediction in concentrated alloys," Materialia **26**, 101620 (2022).
[58]G. Kresse and J. Furthmüller, "Efficiency of ab-initio total energy calculations for metals and semiconductors using a plane-wave basis set," Comput. Mater. Sci. **6**, 15–50 (1996).
[59]J. Furthmüller, J. Hafner, and G. Kresse, "Dimer reconstruction and electronic surface states on clean and hydrogenated diamond (100) surfaces," Phys. Rev. B **53**, 7334 (1996).
[60]G. Kresse and D. Joubert, "From ultrasoft pseudopotentials to the projector augmented-wave method," Phys. Rev. B **59**, 1758–1775 (1999).
[61]J. P. Perdew, K. Burke, and M. Ernzerhof, "Generalized gradient approximation made simple," Phys. Rev. Lett. **77**, 3865–3868 (1996).
[62]A. P. Thompson *et al.*, "LAMMPS-a flexible simulation tool for particle-based materials modeling at the atomic, meso, and continuum scales," Comput. Phys. Commun. **271**, 108171 (2022).
[63]J. M. Cowley, "Short- and long-range order parameters in disordered solid solutions," Phys. Rev. **120**, 1648–1657 (1960).
[64]K. Momma and F. Izumi, "*VESTA*: A three-dimensional visualization system for electronic and structural analysis," J. Appl. Crystallogr. **41**, 653–658 (2008).
[65]N. Iwashita, "X-ray powder diffraction," in *Materials Science and Engineering of Carbon* (Elsevier, 2016), pp. 7–25.
[66]N. Zhou *et al.*, "Single-phase high-entropy intermetallic compounds (HEICs): Bridging high-entropy alloys and ceramics," Sci. Bull. **64**, 856–864 (2019).
[67]G. Henkelman, B. P. Uberuaga, and H. Jónsson, "A climbing image nudged elastic band method for finding saddle points and minimum energy paths," J. Chem. Phys. **113**, 9901–9904 (2000).
[68]A. Manzoor *et al.*, "Machine learning based methodology to predict point defect energies in multi-principal element alloys," Front. Mater. **8**, 129 (2021).
[69]X. G. Li, C. Chen, H. Zheng, Y. Zuo, and S. P. Ong, "Complex strengthening mechanisms in the NbMoTaW multi-principal element alloy," npj Comput. Mater. **6** (2020).
[70]A. Jain *et al.*, "Commentary: The materials project: A materials genome approach to accelerating materials innovation," APL Mater. **1**, 011002 (2013).
[71]S. Zhao, "Local ordering tendency in body-centered cubic (BCC) multi-principal element alloys," J. Phase Equilib. Diffus. **42**, 578–591 (2021).
[72]Y. Li *et al.*, "Chemical ordering effect on the radiation resistance of a CoNiCrFeMn high-entropy alloy," Comput. Mater. Sci. **214**, 111764 (2022).
[73]B. Xing, X. Wang, W. J. Bowman, and P. Cao, "Short-range order localizing diffusion in multi-principal element alloys," Scr. Mater. **210**, 114450 (2022).
[74]D. Frenkel and B. Smit, *Understanding Molecular Simulation: From Algorithms to Applications* (Elsevier, 2023).